A Trajectory Tracking Algorithm for the LSMS Family of Cable-Driven Cranes

Javier Puig-Navarro*, Dominic R. Bisio†, John E. Pye†, Yotam Granov†, Joshua N. Moser†, Jessica S. Friz†, Walter J. Waltz†, Julia Cline†, and B. Danette Allen†
*Analytical Mechannics Associates, Hampton, Virginia, USA 23666
†NASA Langley Research Center, Hampton, Virginia, USA 23666

***Abstract*—The Lightweight Surface Manipulation System, or LSMS, is a family of scalable long-reach cable-actuated manipulators. The design of the LSMS has a high payload ratio for efficient operations on planetary surfaces like the Moon or Mars. The LSMS has nonlinear, coupled, and hybrid dynamics. The engineering decisions that led to these challenging dynamics make this structure light and efficient. This paper proposes a novel trajectory tracking algorithm for these cranes that facilitates precise autonomous and teleoperated operations. This algorithm enables these robots to follow complex trajectories that avoid obstacles and pickup regolith in a construction site.**

I. Introduction

The Lightweight Surface Manipulation System, or LSMS, is a family of long-reach cable-actuated manipulators. Their structure is specifically designed for a multitude of planetary surface operations [1], like the construction of a lunar safe haven [2]. The LSMS family has a high payload ratio, and the ability to scale up dimensions and actuators linearly [3]. The smallest crane within the family is the LSMS-L35. It has a 35-kg lift capacity in lunar gravity [4], and is sized for the Commercial Lunar Payload Services (CLPS) mission landers [5]. The largest robot is the LSMS-1000. It has a 1000-kg lift capacity in lunar gravity [6], and is sized for the Blue Moon lander [7]. Different robots within the LSMS family are available to government agencies, industry, and academia [8].

Serial cable-actuated manipulators, like the LSMS, can accommodate all actuators on their base link. This helps reduce the power of their motors and the mass of the overall structure. Nonetheless, this introduces challenges in the routing of the cables and poses an interesting control problem. *How to move these cables to track an arbitrary trajectory in a complex environment*. Some of the challenges addressed in this paper can be anticipated from Figure 1: i) the nonlinearities caused by the geometry of the cables; ii) the use of spreaders to distribute the loads in different configurations leads to discrete switches in the crane dynamics [9], see points D, H and I; iii) the coupling in the movement of different joint angles, since reeling in a single cable can lead to angle movements in multiple joints; and iv) maintaining tension on the cables to retain controllability of the joint angles.

The work in [10] provides an overview of different lunar cranes, and a brief comparison to Earth crane technologies. Gantry cranes are simple, and present excellent tip-over stability. This type of cranes are commonly found in industrial sites [11]. Recent developments in house printing technologies have lead to the advancement of algorithms for their use in robotic applications. As a result, there is a variety of trajectory tracking algorithms for gantry cranes. Some even leverage the dynamics of a spherical pendulum to model the payload movement [12, 13]. However, these cranes are not a cost-effective solution for lunar and martian operations, due to their reduced payload ratio. Cranes with a small form factor, like the articulated cranes in the LSMS family [14] or the

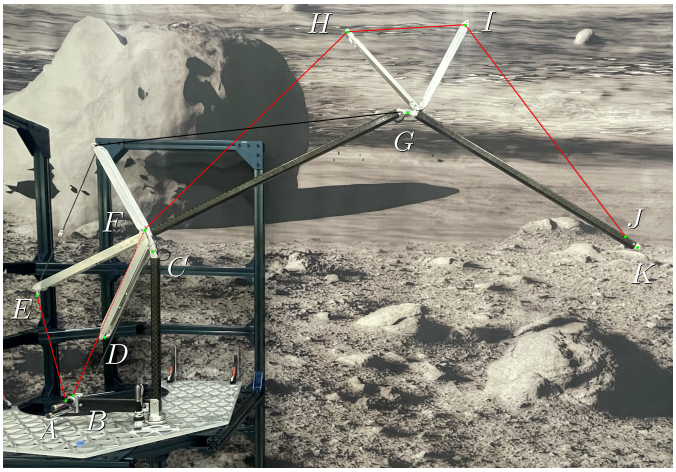

Fig. 1: LSMS-L35 mounted on a mock-up of the payload deck of a Peregrine lander [5], in front of a lunar backdrop. Actuated cables are highlighted in red, whereas non-actuated cables are highlighted in black for visibility. Relevant points in the structure are labeled using capital letters, and their exact position is highlighted by a small green dot: A and B mark the location of the cable spools; C and G correspond to the shoulder and elbow joints; F defines the position of an internal pulley, which is used to route cable B; E and J are cable attachment points; K marks the position of the end effector; and D, H and I denote the location of the pulleys at the end of the spreaders. The function of these spreaders is twofold: i) the efficient distribution of loads under different crane configurations, and ii) managing the cable geometry, which extends the range of operation of the LSMS and enables its use as a manipulator. As the LSMS moves, the pulleys on spreaders D, H and I rest against or lift off from the cables, changing the spreader configuration.

tower crane 34K by Liebherr [15], can be easily packaged and deployed, specially if they are self erecting. This provides a significant advantage on a planetary surface where humans may not be present. Lattice boom cranes, a common sight in large construction projects, share some similarities with the LSMS, such as cable actuation. However, lattice boom cranes tend to operate with much larger payloads. The operations of Earth-based construction cranes always involve human drivers. Some examples are the tower cranes by Liebherr [16], and the lattice boom cranes by Manitowoc [17] or Kobelco [18]. Equipped with sophisticated algorithms, these platforms can dampen payload oscillations [19], and precisely place large payloads where the operator desires [20]. Unlike the LSMS, these cranes are not designed to operate as a serial manipulator. Accordingly, tracking algorithms for complex trajectories are not publicly available for serial cable-actuated cranes.

Relevant work in [21] proposes a general autonomy framework to address critical technology gaps in advanced robotics and autonomous payload handling, identified by NASA Space Technology Mission Directorate and the Exploration Systems Development Mission Directorate in [22, 23]. The algorithm proposed here enables serial tension-actuated manipulators to autonomously follow arbitrary trajectories with precision. To the best of the authors' knowledge, there is no previous algorithm that accomplishes this objective for the LSMS family. This paper presents two main contributions: i) the derivation of the system dynamics for the LSMS robots, which are nonlinear, coupled and hybrid; and ii) the design of a nonlinear trajectory tracking algorithm with formal guarantees that leverages these dynamics. This paper uses Lyapunov and switched systems theory [24, 25] to design a control law with exponential stability under ideal conditions. Later in the text, this result is extended to non-ideal conditions, with uncertainties in the geometry of the LSMS and tracking errors in the motors. These perturbations are propagated through the error dynamics to derive transient and steady-state performance bounds.

The paper is structured as follows. Section II presents the geometric model used to design the algorithm. Section III proposes a novel trajectory tracking algorithm and analyzes its stability. Performance bounds are provided under both ideal and realistic assumptions. Section IV shows the test results on the LSMS-L35. Section V closes the paper with a summary of the theoretical results and their comparison to hardware tests.

II. LSMS MODEL

Given a complex trajectory, specifying desired joint angles and rates as a function of time, the task is to design motor commands and cable movements to track the trajectory. To this end, consider the geometric model of the LSMS illustrated in Figure 2. All passive structural elements are depicted in black, whereas actuated cables are colored in red. The cable that controls the shoulder is attached to the structure at point E, and the cable for the elbow is only attached at point J. Reference frames are color coded using red, green, and blue for the x, y, and z axes, respectively. The ground reference frame $\{\mathcal{G}\}$ is located at the base of the LSMS and is aligned with the north-east-down axes. Each joint has a reference frame attached, which only rotates about its z axis. The x axis of the waist frame $\{0\}$ is aligned with the plane of the LSMS, and its rotation about the z axis with respect to $\{\mathcal{G}\}$ is denoted by angle θ_0. The shoulder is assigned frame $\{1\}$, and the rotation with respect to $\{0\}$ is given by θ_1. The elbow has frame $\{2\}$, and its rotation with respect to $\{1\}$ is defined by θ_2. These definitions yield the following transformation matrices:

$$\boldsymbol{R}_0^{\mathcal{G}} := \begin{bmatrix} \cos\theta_0 & -\sin\theta_0 & 0 \\ \sin\theta_0 & \cos\theta_0 & 0 \\ 0 & 0 & 1 \end{bmatrix}, \quad \boldsymbol{R}_1^0 := \begin{bmatrix} \cos\theta_1 & -\sin\theta_1 & 0 \\ 0 & 0 & 1 \\ -\sin\theta_1 & -\cos\theta_1 & 0 \end{bmatrix}, \quad \boldsymbol{R}_2^1 := \begin{bmatrix} \cos\theta_2 & -\sin\theta_2 & 0 \\ \sin\theta_2 & \cos\theta_2 & 0 \\ 0 & 0 & 1 \end{bmatrix} \in SO(3). \tag{1}$$

Note that $\boldsymbol{R}_1^0$ is the result of two rotations: i) about axis $\boldsymbol{z}$ by an angle θ_1; and ii) about axis $\boldsymbol{x}$ by an angle of -90 degrees.

The LSMS is equipped with three motors located at points 0, A, and B, with gear ratios i_0, i_A, and i_B. The first motor controls the waist. The last two motors, A and B, control the cable lengths, ℓ_A and ℓ_B. Each of these motor has a spool with radii r_A and r_B.

To find the relation between the joint angles and the cable lengths use the geometry detailed in Figures 3 and 4. Figure 3 shows the geometry of cable A for two configurations, depending on whether spreader D is load-bearing. Spreader D is load-bearing when cable A rests against its pulley. For simplicity, only the geometric elements that are relevant are shown. For instance, Figure 3a does not include spreader D because it is not load-bearing. Unit vectors $\boldsymbol{e}_{\mathbf{0}_x}$ and $\boldsymbol{e}_{\mathbf{0}_z}$ in Figure 3

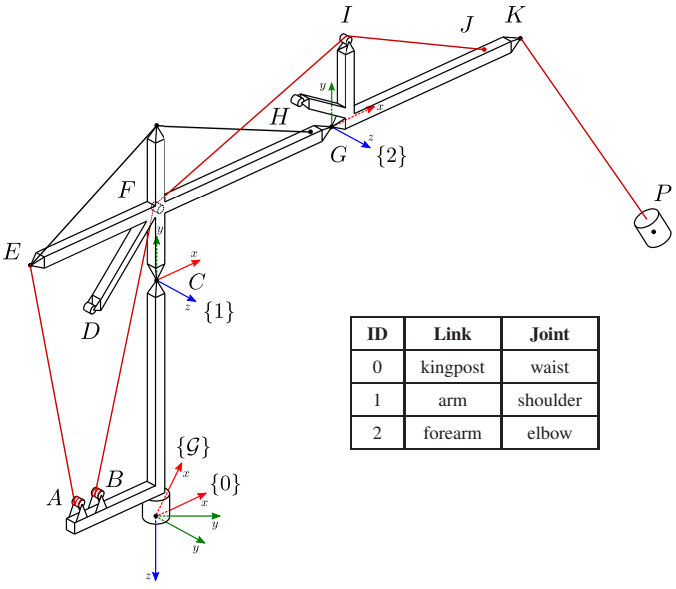

ID	Link	Joint
0	kingpost	waist
1	arm	shoulder
2	forearm	elbow

Fig. 2: Schematic of the LSMS. The legend includes the link and joint names. Actuated cables are depicted in red, whereas structural passive cables are shown in black. Reference frames $\{\mathcal{G}\}$, $\{0\}$, $\{1\}$ and $\{2\}$ are the ground, waist, shoulder, and elbow joint frames. Note that the origin of frames $\{\mathcal{G}\}$ and $\{0\}$ is coincident. They are color coded using red, green, and blue for the x, y, and z axes, respectively.

represent the x and z axes of frame $\{0\}$, translated to point C. Vectors $\boldsymbol{e}_{\mathbf{1}_x}$ and $\boldsymbol{e}_{\mathbf{1}_y}$ denote the x and y axes of frame $\{1\}$. Similarly, Figure 4 depicts the geometry of cable B for three different configurations, depending on whether spreaders H and I are load-bearing. Constant distances between two points X and Y are denoted by d_{XY}, whereas cable lengths that vary with θ_1 and θ_2 are ℓ_{XY}.

The total length of cables A and B is summarized in Tables I and II for the different spreader configurations. All variables ℓ_{XY} contributing to the total lengths ℓ_A and ℓ_B can be expressed using the law of cosines as a function of θ_1 and θ_2 as follows.

$$\begin{aligned}
\ell_{AE}^2(\theta_1) &= d_{AC}^2 + d_{CE}^2 - 2\,d_{AC}\,d_{CE}\cos\alpha_a(\theta_1),\\
\ell_{AD}^2(\theta_1) &= d_{AC}^2 + d_{CD}^2 - 2\,d_{AC}\,d_{CD}\cos\alpha_b(\theta_1),\\
\ell_{BF}^2(\theta_1) &= d_{BC}^2 + d_{CF}^2 - 2\,d_{BC}\,d_{CF}\cos\gamma(\theta_1),\\
\ell_{FJ}^2(\theta_2) &= d_{FG}^2 + d_{GJ}^2 - 2\,d_{FG}\,d_{GJ}\cos\beta_a(\theta_2),\\
\ell_{FI}^2(\theta_2) &= d_{FG}^2 + d_{GI}^2 - 2\,d_{FG}\,d_{GI}\cos\beta_b(\theta_2),\\
\ell_{FH}^2(\theta_2) &= d_{FG}^2 + d_{GH}^2 - 2\,d_{FG}\,d_{GH}\cos\beta_c(\theta_2),
\end{aligned} \tag{2}$$

where the angles on the right-hand side of this equation are

$$\begin{aligned}
\alpha_a(\theta_1) &:= 2\pi - \theta_A - \theta_E - \theta_1,\\
\alpha_b(\theta_1) &:= 2\pi - \theta_A - \theta_D - \theta_1,\\
\gamma(\theta_1) &:= 2\pi - \theta_B - \theta_{F_1} - \theta_1,\\
\beta_a(\theta_2) &:= 2\pi - \theta_J - \theta_{F_2} - \theta_2,\\
\beta_b(\theta_2) &:= 2\pi - \theta_I - \theta_{F_2} - \theta_2,\\
\beta_c(\theta_2) &:= 2\pi - \theta_H - \theta_{F_2} - \theta_2.
\end{aligned} \tag{3}$$

See Figure 3 for the definition of the structural angles θ_A, θ_D, and θ_E; and Figure 4 for θ_B, θ_{F_1}, θ_{F_2}, θ_H, θ_I, and θ_J. The following section derives the transition angles between the different spreader configurations in Figures 3 and 4.

TABLE I: Length of cable A.

Configuration	**(a)**	**(b)**
Contact with D	No	Yes
Condition	$\theta_1 \geq \theta_1^*$	$\theta_1 < \theta_1^*$
$\ell_A(\theta_1)$	ℓ_{AE}	$\ell_{AD} + d_{DE}$
$\dot{\ell}_A(\theta_1)$	$\dot{\ell}_{AE}$	$\dot{\ell}_{AD}$

TABLE II: Length of cable B.

Configuration	**(a)**	**(b)**	**(c)**
Contact with H	No	No	Yes
Contact with I	No	Yes	Yes
Condition	$\theta_2 \geq \theta_2^*$	$\theta_2^{**} \leq \theta_2 < \theta_2^*$	$\theta_2 < \theta_2^{**}$
$\ell_B(\theta_1, \theta_2)$	$\ell_{BF} + \ell_{FJ}$	$\ell_{BF} + \ell_{FI} + d_{IJ}$	$\ell_{BF} + \ell_{FH} + d_{HI} + d_{IJ}$
$\dot{\ell}_B(\theta_1, \theta_2)$	$\dot{\ell}_{BF} + \dot{\ell}_{FJ}$	$\dot{\ell}_{BF} + \dot{\ell}_{FI}$	$\dot{\ell}_{BF} + \dot{\ell}_{FH}$

A. Transition Angles

To find the angle θ_1^* that marks the transition between configurations (a) and (b) in Figure 3, consider vectors ${}^{z}\boldsymbol{v}_{XY}$ from point X to point Y on the LSMS, expressed in reference frame $\{\mathcal{Z}\}$. Then, the following equation ensures that points A, D, and E are colinear, and point D is between A and E:

$$\theta_1^* := \{\theta_1 \mid \det(M_1^*) = 0 \ \wedge \ {}^{1}\boldsymbol{v}_{AD} \cdot {}^{1}\boldsymbol{v}_{DE} > 0\}, \tag{4}$$

where the columns of matrix M_1^* contain the LSMS in-plane components of vectors ${}^{1}\boldsymbol{v}_{AD}$ and ${}^{1}\boldsymbol{v}_{DE}$, that is

$$M_1^* := \left[\begin{smallmatrix} 1 & 0 & 0 \\ 0 & 1 & 0 \end{smallmatrix}\right] \left[{}^{1}\boldsymbol{v}_{AD}, {}^{1}\boldsymbol{v}_{DE}\right]. \tag{5}$$

Since ${}^{1}\boldsymbol{v}_{AD} = \boldsymbol{R}_1^{0\top}\,{}^{0}\boldsymbol{v}_{AC} + {}^{1}\boldsymbol{v}_{CD}$, the determinant in Equation (4) yields an equality of the form

$$a_1^* \cos\theta_1 + b_1^* \sin\theta_1 = c_1^*, \tag{6}$$

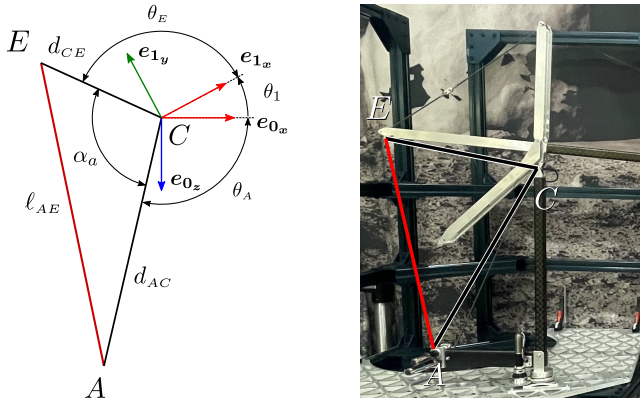

(a) Cable A does not rest against pulley D when $\theta_1 \geq \theta_1^*$.

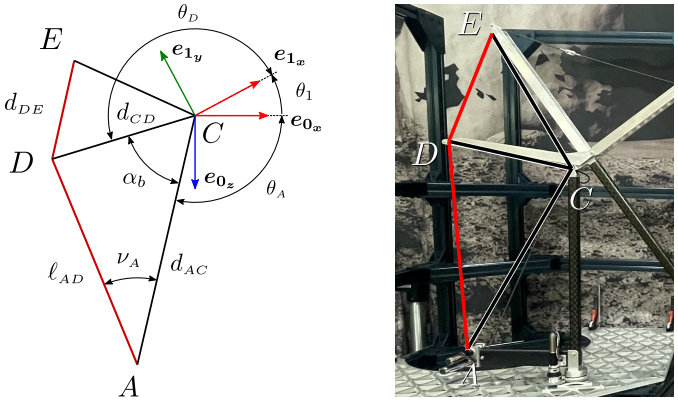

(b) Cable A rests against pulley D when $\theta_1 < \theta_1^*$.

Fig. 3: Geometry of cable A. The left column shows schematics with relevant parameters in the derivation of the length of cable A. The right column shows a simplified version of these schematics overlaid on a picture of the LSMS-L35. Only the kingpost and part of the arm are shown in these images. Note that the black segments in these diagrams do not depict the struts of the LSMS, but vectors between two relevant points on the same link.

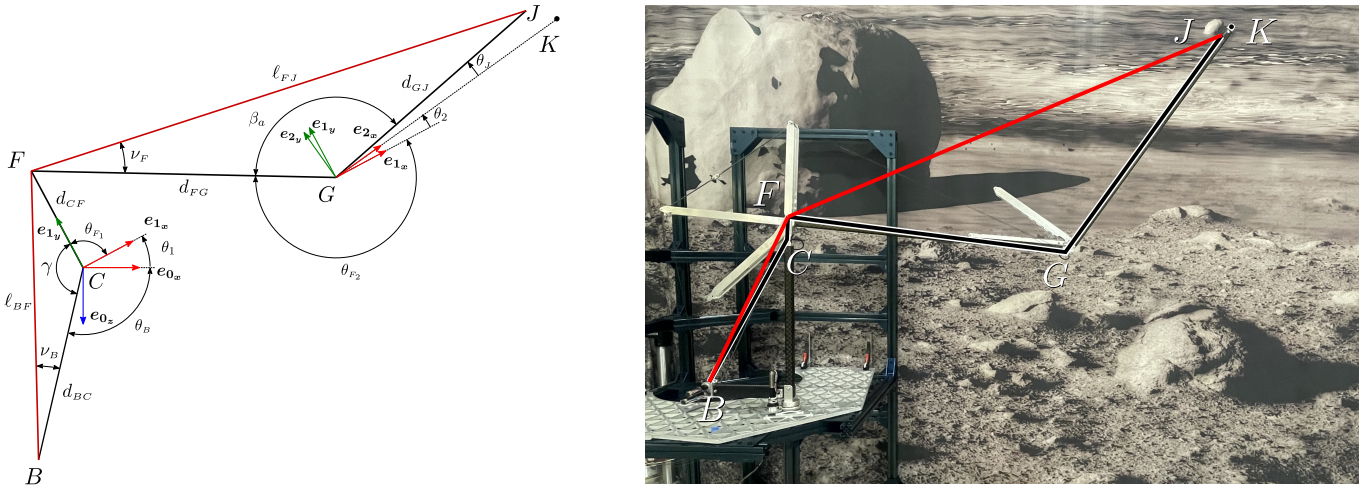

(a) Cable B only rests against pulley F when $\theta_2 \geq \theta_2^*$.

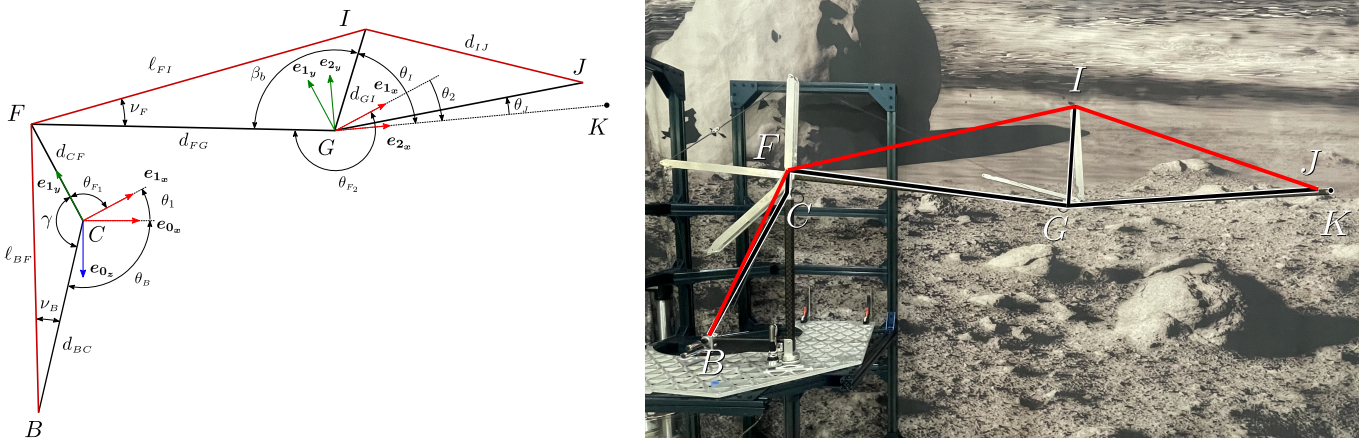

(b) Cable B rests against pulleys F and I when $\theta_2^{**} \leq \theta_2 < \theta_2^*$.

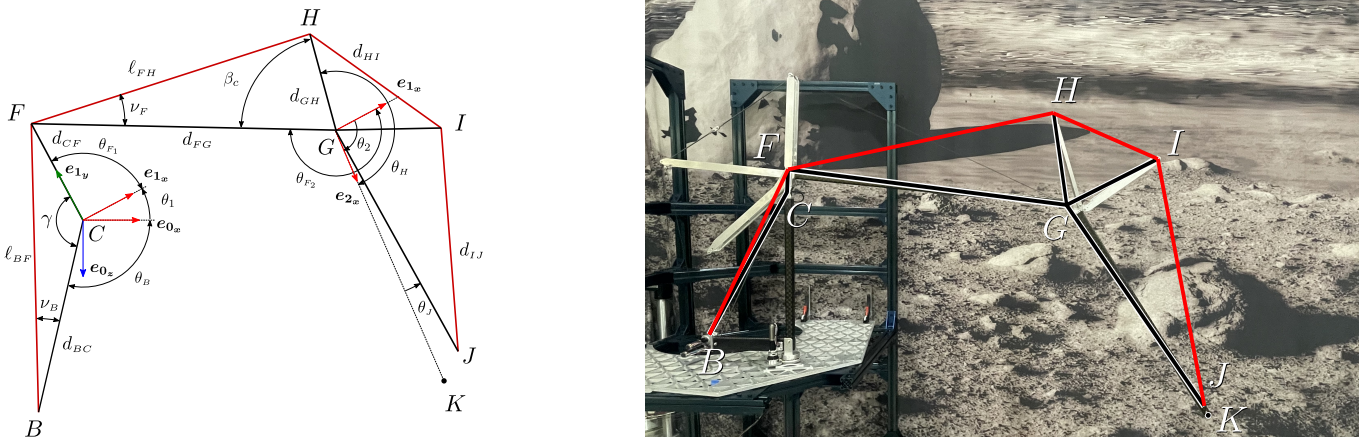

(c) Cable B rests against pulleys F, H and I when $\theta_2 < \theta_2^{**}$.

Fig. 4: Geometry of cable B. The left column shows schematics with relevant parameters in the derivation of the length of cable B. The right column shows a simplified version of these schematics overlaid on a picture of the LSMS-L35. Note that the black segments in these diagrams do not depict the struts of the LSMS, but vectors between two relevant points on the same link. Some angles and distances in the schematics have been distorted to fit the symbols for the relevant parameters. Compare, for example, the distance between points C and F or angle γ on the left and right columns.

with constant coefficients a_1^*, b_1^*, and c_1^*, fully defined by the geometry of the LSMS

$$\begin{aligned} a_1^* &:= {}^0\boldsymbol{v}_{\boldsymbol{AC}}^\top \begin{bmatrix} 0 & 1 & 0 \\ 0 & 0 & 0 \\ 1 & 0 & 0 \end{bmatrix} {}^1\boldsymbol{v}_{DE}, \quad b_1^* := {}^0\boldsymbol{v}_{\boldsymbol{AC}}^\top \begin{bmatrix} 1 & 0 & 0 \\ 0 & 0 & 0 \\ 0 & -1 & 0 \end{bmatrix} {}^1\boldsymbol{v}_{DE}, \\ c_1^* &:= {}^1\boldsymbol{v}_{\boldsymbol{CD}}^\top \begin{bmatrix} 0 & -1 & 0 \\ 1 & 0 & 0 \\ 0 & 0 & 0 \end{bmatrix} {}^1\boldsymbol{v}_{DE}. \end{aligned} \tag{7}$$

Equation (6) has two closed-form solutions, which can be obtained with the change of variables $a_1^* = r\cos\alpha$ and $b_1^* = r\sin\alpha$ as

$$\theta_{1_{\{1,2\}}}^* = \operatorname{atan2}\left(b_1^*, a_1^*\right) \pm \operatorname{acos}\left(c_1^* \left(a_1^{*2} + b_1^{*2}\right)^{-\frac{1}{2}}\right). \tag{8}$$

The correct solution θ_1^* can be identified by checking the second condition in Equation (4). Repeating the same procedure for spreaders H and I yields θ_2^* and θ_2^{**}, the transition angles between configurations (a) and (b), and (b) and (c), shown in Figure 4.

$$\begin{aligned} \theta_2^* &:= \{\theta_2 \mid \det(M_2^*) = 0 \ \wedge \ {}^2\boldsymbol{v}_{FI} \cdot {}^2\boldsymbol{v}_{IJ} > 0\}, \\ \theta_2^{**} &:= \{\theta_2 \mid \det(M_2^{**}) = 0 \ \wedge \ {}^2\boldsymbol{v}_{FH} \cdot {}^2\boldsymbol{v}_{HI} > 0\}, \end{aligned} \tag{9}$$

where matrices M_2^* and M_2^{**} are

$$M_2^* := \begin{bmatrix} 1 & 0 & 0 \\ 0 & 1 & 0 \end{bmatrix} \left[{}^2\boldsymbol{v}_{FI}, {}^2\boldsymbol{v}_{IJ}\right], \quad M_2^{**} := \begin{bmatrix} 1 & 0 & 0 \\ 0 & 1 & 0 \end{bmatrix} \left[{}^2\boldsymbol{v}_{FH}, {}^2\boldsymbol{v}_{HI}\right]. \tag{10}$$

The correct solutions can be retrieved from the following expressions, by checking which solutions meet the second conditions in Equation (9):

$$\begin{aligned} \theta_{2_{\{1,2\}}}^* &= \operatorname{atan2}\left(b_2^*, a_2^*\right) \pm \operatorname{acos}\left(c_2^* \left(a_2^{*2} + b_2^{*2}\right)^{-\frac{1}{2}}\right), \\ \theta_{2_{\{1,2\}}}^{**} &= \operatorname{atan2}\left(b_2^{**}, a_2^{**}\right) \pm \operatorname{acos}\left(c_2^{**} \left(a_2^{**2} + b_2^{**2}\right)^{-\frac{1}{2}}\right), \end{aligned} \tag{11}$$

with constant coefficients

$$\begin{aligned} a_2^* &:= {}^1\boldsymbol{v}_{\boldsymbol{FG}}^\top \begin{bmatrix} 0 & 1 & 0 \\ -1 & 0 & 0 \\ 0 & 0 & 0 \end{bmatrix} {}^2\boldsymbol{v}_{IJ}, \quad b_2^* := {}^1\boldsymbol{v}_{\boldsymbol{FG}}^\top \begin{bmatrix} 1 & 0 & 0 \\ 0 & 1 & 0 \\ 0 & 0 & 0 \end{bmatrix} {}^2\boldsymbol{v}_{IJ}, \\ c_2^* &:= {}^2\boldsymbol{v}_{\boldsymbol{GI}}^\top \begin{bmatrix} 0 & -1 & 0 \\ 1 & 0 & 0 \\ 0 & 0 & 0 \end{bmatrix} {}^2\boldsymbol{v}_{IJ}, \quad a_2^{**} := {}^1\boldsymbol{v}_{\boldsymbol{FG}}^\top \begin{bmatrix} 0 & 1 & 0 \\ -1 & 0 & 0 \\ 0 & 0 & 0 \end{bmatrix} {}^2\boldsymbol{v}_{HI}, \\ b_2^{**} &:= {}^1\boldsymbol{v}_{\boldsymbol{FG}}^\top \begin{bmatrix} 1 & 0 & 0 \\ 0 & 1 & 0 \\ 0 & 0 & 0 \end{bmatrix} {}^2\boldsymbol{v}_{HI}, \quad c_2^{**} := {}^2\boldsymbol{v}_{\boldsymbol{GH}}^\top \begin{bmatrix} 0 & -1 & 0 \\ 1 & 0 & 0 \\ 0 & 0 & 0 \end{bmatrix} {}^2\boldsymbol{v}_{HI}. \end{aligned} \tag{12}$$

III. Trajectory Tracking Control

To control the geometry of the LSMS, the temporal evolution of the cable lengths can be expressed as a function of the motor angular speeds ω_A and ω_B, the gearbox ratios i_A and i_B, and the spool radii r_A and r_B

$$\dot{\ell}_A = -\omega_A i_A r_A, \qquad \dot{\ell}_B = -\omega_B i_B r_B. \tag{13}$$

The negative signs in Equation (13) imply that positive angular speeds for motors A and B shorten the corresponding cable lengths. This sign is chosen to match the hardware sign convention of the LSMS. The time evolution of the different cable segments are given in Tables I and II, and yield the following time derivatives of Equation (2):

$$\begin{aligned} \ell_{AE}\,\dot{\ell}_{AE} &= -d_{AC}\,d_{CE}\,\dot{\theta}_1 \sin\alpha_a(\theta_1), \\ \ell_{AD}\,\dot{\ell}_{AD} &= -d_{AC}\,d_{CD}\,\dot{\theta}_1 \sin\alpha_b(\theta_1), \\ \ell_{BF}\,\dot{\ell}_{BF} &= -d_{BC}\,d_{CF}\,\dot{\theta}_1 \sin\gamma(\theta_1), \\ \ell_{FJ}\,\dot{\ell}_{FJ} &= -d_{FG}\,d_{GJ}\,\dot{\theta}_2 \sin\beta_a(\theta_2), \\ \ell_{FI}\,\dot{\ell}_{FI} &= -d_{FG}\,d_{GI}\,\dot{\theta}_2 \sin\beta_b(\theta_2), \\ \ell_{FH}\,\dot{\ell}_{FH} &= -d_{FG}\,d_{GH}\,\dot{\theta}_2 \sin\beta_c(\theta_2). \end{aligned} \tag{14}$$

To control the off-plane motion of the LSMS, an electrical motor drives the waist with angular speed ω_0. Define the vector of angular speeds $\boldsymbol{\omega} := [\omega_0, \omega_A, \omega_B]^\top$ and the vector of joint errors $\boldsymbol{e_\theta} := [e_{\theta_0}, e_{\theta_1}, e_{\theta_2}]^\top$ with

$$e_{\theta_i} := \theta_i - \theta_{d_i}, \qquad i \in \{0, 1, 2\}, \tag{15}$$

where θ_{d_i} denotes the desired angle for the ith joint of the LSMS. The terms θ_{d_i} are time-parameterized, and are provided by an algorithm that can generate safe and feasible trajectories for the LSMS. Then, the control objective is to solve the following problem:

Definition 1 (Trajectory tracking problem): Design angular speed commands $\boldsymbol{\omega_c} := [\omega_{0_c}, \omega_{A_c}, \omega_{B_c}]^\top$ to drive the joint error $\boldsymbol{e_\theta}$ to the origin

$$\|\boldsymbol{e_\theta}\| \overset{t\to\infty}{\longrightarrow} 0. \tag{16}$$

To maintain the LSMS in a safe and controllable state, consider the following assumption:

Assumption 1: Cables A and B remain under tension.

Violating Assumption 1 can lead to the sudden collapse of the forearm onto the arm, or even the tipping of the arm over the kingpost. The lack of tension on these cables makes the shoulder and elbow angles not controllable. To guarantee that Assumption 1 is met, the LSMS implements an envelope protection algorithm in the trajectory generation phase. This ensures $\boldsymbol{\theta} := [\theta_0, \theta_1, \theta_2] \in \Omega_s$, where Ω_s is the set of angles for which the LSMS is safe and controllable. Equations (2) and (14) implicitly consider Assumption 1. For simplicity, consider also the following assumptions:

Assumption 2: Fixed distances d_{XY} and angles θ_Z that describe the geometry of the LSMS are known precisely with

$$\begin{aligned} (X, Y) \in \{&(A, C), (B, C), (C, D), (C, E), (C, F), \\ &(F, G), (G, H), (G, I), (G, J)\}, \\ Z \in \{&A, B, D, E, F_1, F_2, H, I, J\}. \end{aligned} \tag{17}$$

Assumption 3: The underlying motor controllers can track the angular speed commands precisely, that is $\boldsymbol{\omega} \equiv \boldsymbol{\omega_c}$.

The consequences of violating Assumptions 2 and 3 are addressed in Section III-A.

Next, combine Equations (13) and (14) with the last rows in Tables I and II to derive the temporal evolution of the joint angles in Equations (18), (19), and (20).

$$\dot{\theta}_0 = i_0 \omega_0, \tag{18}$$

$$\dot{\theta}_1 = \begin{cases} \dfrac{i_A r_A}{d_{AC}\,d_{CE}} \dfrac{\ell_{AE}}{\sin\alpha_a}\,\omega_A, & \text{if } \theta_1 \geq \theta_1^*, \\ \dfrac{i_A r_A}{d_{AC}\,d_{CD}} \dfrac{\ell_{AD}}{\sin\alpha_b}\,\omega_A, & \text{if } \theta_1 < \theta_1^*. \end{cases} \tag{19}$$

The equations of motion for θ_1 and θ_2 are coupled, nonlinear, and present discrete switches due to the different spreader configurations. The two configurations of spreader D and the three configurations of spreaders H and I produce a total of six switching conditions for $\dot{\theta}_2$. The terms n_a and n_b in Equation (20) are dimensionless quantities that characterize

$$\dot{\theta}_2 = \begin{cases} \dfrac{1}{d_{FG}\, d_{GJ}} \dfrac{\ell_{FJ}(\theta_2)}{\sin\beta_a(\theta_2)} \left(n_a(\theta_1)\, i_A r_A\, \omega_A + i_B r_B\, \omega_B\right), & \text{if } \theta_1 \geq \theta_1^* \wedge \theta_2 \geq \theta_2^*, \\ \dfrac{1}{d_{FG}\, d_{GI}} \dfrac{\ell_{FI}(\theta_2)}{\sin\beta_b(\theta_2)} \left(n_a(\theta_1)\, i_A r_A\, \omega_A + i_B r_B\, \omega_B\right), & \text{if } \theta_1 \geq \theta_1^* \wedge \theta_2^{**} \leq \theta_2 < \theta_2^*, \\ \dfrac{1}{d_{FG}\, d_{GH}} \dfrac{\ell_{FH}(\theta_2)}{\sin\beta_c(\theta_2)} \left(n_a(\theta_1)\, i_A r_A\, \omega_A + i_B r_B\, \omega_B\right), & \text{if } \theta_1 \geq \theta_1^* \wedge \theta_2 < \theta_2^{**}, \\ \dfrac{1}{d_{FG}\, d_{GJ}} \dfrac{\ell_{FJ}(\theta_2)}{\sin\beta_a(\theta_2)} \left(n_b(\theta_1)\, i_A r_A\, \omega_A + i_B r_B\, \omega_B\right), & \text{if } \theta_1 < \theta_1^* \wedge \theta_2 \geq \theta_2^*, \\ \dfrac{1}{d_{FG}\, d_{GI}} \dfrac{\ell_{FI}(\theta_2)}{\sin\beta_b(\theta_2)} \left(n_b(\theta_1)\, i_A r_A\, \omega_A + i_B r_B\, \omega_B\right), & \text{if } \theta_1 < \theta_1^* \wedge \theta_2^{**} \leq \theta_2 < \theta_2^*, \\ \dfrac{1}{d_{FG}\, d_{GH}} \dfrac{\ell_{FH}(\theta_2)}{\sin\beta_c(\theta_2)} \left(n_b(\theta_1)\, i_A r_A\, \omega_A + i_B r_B\, \omega_B\right), & \text{if } \theta_1 < \theta_1^* \wedge \theta_2 < \theta_2^{**}. \end{cases} \tag{20}$$

the coupling between θ_1 and θ_2, for configurations (a) and (b) of spreader D shown in Figure 3.

$$\begin{aligned} n_a(\theta_1) &:= -\frac{d_{BC}\, d_{CF}}{d_{AC}\, d_{CE}} \frac{\ell_{AE}(\theta_1)}{\ell_{BF}(\theta_1)} \frac{\sin\gamma(\theta_1)}{\sin\alpha_a(\theta_1)}, \\ n_b(\theta_1) &:= -\frac{d_{BC}\, d_{CF}}{d_{AC}\, d_{CD}} \frac{\ell_{AD}(\theta_1)}{\ell_{BF}(\theta_1)} \frac{\sin\gamma(\theta_1)}{\sin\alpha_b(\theta_1)}. \end{aligned} \tag{21}$$

Since n_a and n_b are negative for all $\boldsymbol{\theta} \in \Omega_s$, if ℓ_A is shortened, that is $\omega_A > 0$, and ℓ_B is kept constant, that is $\omega_B = 0$, then θ_2 decreases while θ_1 increases, as expected from the geometry in Figure 4. Next, the error dynamics can be expressed as

$$\dot{\boldsymbol{e}}_{\boldsymbol{\theta}} = [\dot{\theta}_0 - \dot{\theta}_{d_0}, \dot{\theta}_1 - \dot{\theta}_{d_1}, \dot{\theta}_2 - \dot{\theta}_{d_2}]^\top. \tag{22}$$

To solve the trajectory tracking problem consider the control laws in Equations (23), (24), and (27).

$$\omega_{0_c} = \frac{1}{i_0} \left(\dot{\theta}_{d_0} - \kappa_0 e_{\theta_0}\right), \tag{23}$$

$$\omega_{A_c} = \begin{cases} \dfrac{d_{AC}\, d_{CE}}{i_A r_A} \dfrac{\sin\alpha_a}{\ell_{AE}} \left(\dot{\theta}_{d_1} - \kappa_1 e_{\theta_1}\right), & \text{if } \theta_1 \geq \theta_1^*, \\ \dfrac{d_{AC}\, d_{CD}}{i_A r_A} \dfrac{\sin\alpha_b}{\ell_{AD}} \left(\dot{\theta}_{d_1} - \kappa_1 e_{\theta_1}\right), & \text{if } \theta_1 < \theta_1^*. \end{cases} \tag{24}$$

The expression for ω_{0_c} is a linear proportional control with a feedforward term, whereas ω_{A_c} and ω_{B_c} are nonlinear, switched control laws with feedforward terms. The proposed control laws only require three tuning gains: κ_0 for the waist, κ_1 for the shoulder, and κ_2 for the elbow. Lemma 1 proves *uniform exponential stability* of the trajectory tracking errors. It also proves that the proposed protocol decouples the shoulder and error dynamics.

Lemma 1: Assumptions 1, 2 and 3, the error dynamics in (22), and the control laws in Equations (23), (24), and (27) ensure that

$$|e_{\theta_i}(t)| = |e_{\theta_i}(t_0)| e^{-\kappa_i (t - t_0)}, \quad \forall i \in \{0, 1, 2\}, \quad t \geq t_0, \tag{25}$$

with known control gains κ_0, κ_1, and $\kappa_2 > 0$.

Proof: The control laws in (24) and (27) decouple the shoulder and elbow error dynamics, and yield

$$\dot{e}_{\theta_i} = -\kappa_i e_{\theta_i} \Longrightarrow e_{\theta_i}(t) = e_{\theta_i}(t_0) e^{-\kappa_i (t - t_0)}, \tag{26}$$

for all $i \in \{0, 1, 2\}$ and $t \geq t_0$. ■

Since Assumption 1 restricts the range of motion of the LSMS to a safe envelope Ω_s, the result in Lemma 1 proves

$$\omega_{B_c} = \begin{cases} m \left(\dot{\theta}_{d_1} - \kappa_1 e_{\theta_1}\right) + \dfrac{d_{FG}\, d_{GJ}}{i_B r_B} \dfrac{\sin\beta_a}{\ell_{FJ}} \left(\dot{\theta}_{d_2} - \kappa_2 e_{\theta_2}\right), & \text{if } \theta_1 \geq \theta_1^* \wedge \theta_2 \geq \theta_2^*, \\ m \left(\dot{\theta}_{d_1} - \kappa_1 e_{\theta_1}\right) + \dfrac{d_{FG}\, d_{GI}}{i_B r_B} \dfrac{\sin\beta_b}{\ell_{FI}} \left(\dot{\theta}_{d_2} - \kappa_2 e_{\theta_2}\right), & \text{if } \theta_1 \geq \theta_1^* \wedge \theta_2^{**} \leq \theta_2 < \theta_2^*, \\ m \left(\dot{\theta}_{d_1} - \kappa_1 e_{\theta_1}\right) + \dfrac{d_{FG}\, d_{GH}}{i_B r_B} \dfrac{\sin\beta_c}{\ell_{FH}} \left(\dot{\theta}_{d_2} - \kappa_2 e_{\theta_2}\right), & \text{if } \theta_1 \geq \theta_1^* \wedge \theta_2 < \theta_2^{**}, \\ m \left(\dot{\theta}_{d_1} - \kappa_1 e_{\theta_1}\right) + \dfrac{d_{FG}\, d_{GJ}}{i_B r_B} \dfrac{\sin\beta_a}{\ell_{FJ}} \left(\dot{\theta}_{d_2} - \kappa_2 e_{\theta_2}\right), & \text{if } \theta_1 < \theta_1^* \wedge \theta_2 \geq \theta_2^*, \\ m \left(\dot{\theta}_{d_1} - \kappa_1 e_{\theta_1}\right) + \dfrac{d_{FG}\, d_{GI}}{i_B r_B} \dfrac{\sin\beta_b}{\ell_{FI}} \left(\dot{\theta}_{d_2} - \kappa_2 e_{\theta_2}\right), & \text{if } \theta_1 < \theta_1^* \wedge \theta_2^{**} \leq \theta_2 < \theta_2^*, \\ m \left(\dot{\theta}_{d_1} - \kappa_1 e_{\theta_1}\right) + \dfrac{d_{FG}\, d_{GH}}{i_B r_B} \dfrac{\sin\beta_c}{\ell_{FH}} \left(\dot{\theta}_{d_2} - \kappa_2 e_{\theta_2}\right), & \text{if } \theta_1 < \theta_1^* \wedge \theta_2 < \theta_2^{**}, \end{cases} \quad \text{with} \quad m := \frac{d_{BC}\, d_{CF}}{i_B r_B} \frac{\sin\gamma}{\ell_{BF}}. \tag{27}$$

local uniform exponential stability. The following section relaxes Assumptions 2 and 3 to find more realistic performance bounds for the control law.

A. Relaxation of Assumptions 2 and 3

The geometry of the LSMS is subject to modeling and manufacturing errors. As a result, the controller has knowledge of the nominal geometry, which may differ from the real geometry by a bounded tolerance, as detailed in the following assumption:

Assumption 4: Nominal distances d_{XY_o} that characterize the geometry of the LSMS, and angles $0 < \nu_{Z_o} < \pi$ have a known tolerance $0 \leq \epsilon < 1$, satisfying

$$1-\epsilon \leq \frac{d_{XY_o}}{d_{XY}} \leq 1+\epsilon, \quad 1-\epsilon \leq \frac{\sin\nu_{Z_o}}{\sin\nu_Z} \leq 1+\epsilon, \tag{28}$$

for all $(X,Y) \in \{(A,C),(B,C),(F,G)\}$ and all $Z \in \{A,B,F\}$. See Figures 3 and 4 for the definition of ν_A, ν_B, and ν_F.

This assumption lets the control system believe the LSMS has a spreader configuration that may not match the real configuration, as long as the error in the estimation of ν_Z is bounded. Note that Assumption 4 considers that angles ν_Z are bounded away from 0 and π due to the physical design of the LSMS and the envelope protection algorithm, that is $0 < \underline{\nu}_Z \leq \nu_Z \leq \bar{\nu}_Z < \pi$. As a result, the maximum joint errors are also bounded

$$|e_{\theta_i}| \leq \bar{e}_{\theta_0}, \qquad \forall i \in \{0,1,2\}, \tag{29}$$

with $\bar{e}_{\theta_0} := 2\pi$, $\bar{e}_{\theta_1} := \bar{\theta}_1 - \underline{\theta}_1$, and $\bar{e}_{\theta_2} := \bar{\theta}_2 - \underline{\theta}_2$. The upper and lower bounds for θ_1 and θ_2 can be derived using the definition of ν_A and ν_B, see Figures 3 and 4, and the values for $\underline{\nu}_A$ and $\underline{\nu}_F$. The choice of angles $\underline{\nu}_A$ and $\underline{\nu}_F$ is beyond the scope of this paper.

$$\begin{aligned}
\bar{\theta}_1 &:= 2\pi - \theta_A - \theta_E - \bar{f}\left(\frac{d_{AC}}{d_{CE}}, \underline{\nu}_A\right), \\
\underline{\theta}_1 &:= 2\pi - \theta_A - \theta_D - \underline{f}\left(\frac{d_{AC}}{d_{CD}}, \underline{\nu}_A\right), \\
\bar{\theta}_2 &:= \pi - \theta_J - \bar{f}\left(\frac{d_{GJ}}{d_{FJ}}, \underline{\nu}_F\right), \\
\underline{\theta}_2 &:= \pi - \theta_H - \underline{f}\left(\frac{d_{GH}}{d_{FJ}}, \underline{\nu}_F\right).
\end{aligned} \tag{30}$$

Functions $\bar{f}$ and $\underline{f}$ can be obtained combining the law of sines, the law of cosines, and other trigonometric identities, yielding

$$\begin{aligned}
\bar{f}(r,\nu) &:= \operatorname{acos}\left(r\sin^2\nu + \cos\nu\sqrt{1-r^2\sin^2\nu}\right), \\
\underline{f}(r,\nu) &:= \operatorname{acos}\left(r\sin^2\nu - \cos\nu\sqrt{1-r^2\sin^2\nu}\right).
\end{aligned} \tag{31}$$

In addition, the motors have unmodelled dynamics and cannot track the speed commands precisely. Assumption 5 considers a speed tracking error for each motor.

Assumption 5: The underlying motor controllers track the angular speed commands within a bounded error $\delta_i := \omega_i - \omega_{i_c}$

$$|\delta_i| \leq \bar{\delta}_i, \quad i \in \{0,A,B\}. \tag{32}$$

Next, replace the ideal LSMS parameters by the nominal counterparts in the control laws (23), (24), and (27), and substitute into the error dynamics in (22) to arrive at the following expression:

$$\dot{e}_{\theta_0} = -\kappa_0 e_{\theta_0} + i_0\delta_0, \tag{33a}$$

$$\dot{e}_{\theta_1} = -\kappa_1 e_{\theta_1} + \eta_{1,A}\,\delta_A + \eta_{1,1}\left(\dot{\theta}_{d_1} - \kappa_1 e_{\theta_1}\right), \tag{33b}$$

$$\begin{aligned}
\dot{e}_{\theta_2} = &-\kappa_2 e_{\theta_2} + \eta_{2,A}\,\delta_A + \eta_{2,1}\left(\dot{\theta}_{d_1} - \kappa_1 e_{\theta_1}\right) \\
&+ \eta_{2,B}\,\delta_B + \eta_{2,2}\left(\dot{\theta}_{d_2} - \kappa_2 e_{\theta_2}\right),
\end{aligned} \tag{33c}$$

with direct perturbation terms

$$\begin{aligned}
\eta_{1,A} &:= \frac{i_A r_A}{d_{AC}\sin\nu_A}, & \eta_{2,B} &:= \frac{i_B r_B}{d_{FG}\sin\nu_F}, \\
\eta_{1,1} &:= \frac{d_{AC_o}}{d_{AC}}\frac{\sin\nu_{A_o}}{\sin\nu_A} - 1, & \eta_{2,2} &:= \frac{d_{FG_o}}{d_{FG}}\frac{\sin\nu_{F_o}}{\sin\nu_F} - 1,
\end{aligned} \tag{34}$$

and perturbations due to the shoulder-elbow coupling

$$\begin{aligned}
\eta_{2,A} &:= -i_A\frac{r_A d_{BC}}{d_{AC}\,d_{FG}}\frac{\sin\nu_B}{\sin\nu_A\,\sin\nu_F}, \\
\eta_{2,1} &:= \frac{d_{BC}}{d_{FG}}\frac{\sin\nu_B}{\sin\nu_F}\left(\frac{d_{BC_o}}{d_{BC}}\frac{\sin\nu_{B_o}}{\sin\nu_B} - \frac{d_{AC_o}}{d_{AC}}\frac{\sin\nu_{A_o}}{\sin\nu_A}\right).
\end{aligned} \tag{35}$$

Note that angles ν_A, ν_B, and ν_F are shown in Figures 3 and 4, and the terms $\sin\nu_A$, $\sin\nu_B$, and $\sin\nu_F$ above are related to expressions in Equations (19) and (20) as follows.

$$\begin{aligned}
\sin\nu_A &= \begin{cases} \dfrac{d_{CE}\sin\alpha_a}{\ell_{AE}}, & \text{if } \theta_1 \geq \theta_1^*, \\ \dfrac{d_{CD}\sin\alpha_b}{\ell_{AD}}, & \text{if } \theta_1 < \theta_1^*, \end{cases} \\
\sin\nu_B &= \frac{d_{CF}\sin\gamma}{\ell_{BF}}, \\
\sin\nu_F &= \begin{cases} \dfrac{d_{GJ}\sin\beta_a}{\ell_{FJ}}, & \text{if } \theta_2 \geq \theta_2^*, \\ \dfrac{d_{GI}\sin\beta_b}{\ell_{FI}}, & \text{if } \theta_2^{**} \leq \theta_2 < \theta_2^*, \\ \dfrac{d_{GH}\sin\beta_c}{\ell_{FH}}, & \text{if } \theta_2 < \theta_2^{**}. \end{cases}
\end{aligned} \tag{36}$$

Terms $\sin\nu_{A_o}$, $\sin\nu_{B_o}$, and $\sin\nu_{F_o}$ have the same structure. Simply replace the real geometry above with the nominal geometry in Assumption 4 to obtain their expressions.

The next theorems combine perturbation and Lyapunov theory to derive transient and steady-state performance bounds for the trajectory tracking errors. For simplicity, the results are separated into two theorems that capture the waist, and the shoulder-elbow behaviors under non-ideal conditions. The first theorem proves *uniform ultimate boundedness* of the waist trajectory tracking error, see Definition 4.6 in [24].

Theorem 1: Given Assumptions 1, 4, and 5, and the error dynamics in (33a), if conditions

$$|e_{\theta_0}(t_0)| < \rho_0 \quad \text{and} \quad \bar{\delta}_0 < \frac{\kappa_0}{i_0}\mu_0\rho_0 \tag{37}$$

are met with $\rho_0 = \bar{e}_{\theta_0}$ and $0 < \mu_0 < 1$, then there exists a $T_0 \geq 0$ such that

$$\begin{aligned} |e_{\theta_0}(t)| &\leq |e_{\theta_0}(t_0)| e^{-(1-\mu_0)\kappa_0(t-t_0)}, \quad \forall t_0 \leq t < t_0 + T_0, \\ |e_{\theta_0}(t)| &\leq \frac{i_0 \bar{\delta}_0}{\kappa_0 \mu_0}, \qquad\qquad\qquad\quad \forall t \geq t_0 + T_0. \end{aligned} \tag{38}$$

Proof: The theorem above results from the application of Lemma 9.2 in [24] with Lyapunov function $V = \frac{1}{2} e_{\theta_0}^2 > 0$ for all $e_{\theta_0} \neq 0$. ∎

Note that the guaranteed rate of convergence in Theorem 1 approaches that of Lemma 1 as μ_0 approaches 0. However, as μ_0 approaches 0 the ultimate uniform bound increases. In addition, this bound can be made arbitrarily small using a combination of two strategies: i) improving the performance of the waist motor, that is reducing $\bar{\delta}_0$; and ii) increasing the control gain κ_0. In the latter strategy, careful consideration should be given to the drawbacks of high-gain controllers. An upper bound for T_0, which depends on the initial waist error, can be easily derived using Equation (38).

The second theorem shows that under non-ideal conditions the shoulder and elbow error dynamics cannot be fully decoupled, and are uniformly ultimately bounded. To derive these results, define the shoulder-elbow errors $\boldsymbol{e} := [e_{\theta_1}, e_{\theta_2}]^\top$, the motor tracking errors $\boldsymbol{\delta} := [\delta_A, \delta_B]^\top$, and the desired rates $\dot{\boldsymbol{\theta}}_{\boldsymbol{d}} := [\dot{\theta}_{d_1}, \dot{\theta}_{d_2}]^\top$, with known bounds $\|\boldsymbol{\delta}\| \leq \bar{\delta} := (\delta_A^2 + \delta_B^2)^{\frac{1}{2}}$ and $\|\dot{\boldsymbol{\theta}}_{\boldsymbol{d}}\| \leq \dot{\theta}_d$.

Theorem 2: Given Assumptions 1, 4, and 5, and the error dynamics in (33b) and (33c), if conditions

$$\|\boldsymbol{e}(t_0)\| < \rho \quad \text{and} \quad \eta_\delta \, \bar{\delta} + \eta_{\dot{\theta}_d} \bar{\dot{\theta}}_d < \rho \mu \lambda, \tag{39}$$

are met with $\rho = (\bar{e}_{\theta_1}^2 + \bar{e}_{\theta_2}^2)^{\frac{1}{2}}$ and $0 < \mu < 1$, and the control gains satisfy

$$\frac{\kappa_2}{\kappa_1} \geq \frac{4\epsilon^2}{(1-\xi)^2} \frac{(1+\epsilon)^2}{(1-\epsilon)^6} \left(\frac{d_{BC_o}}{d_{FG_o}} \right)^2 \frac{\max\limits_{\nu_B \in [\underline{\nu}_B, \bar{\nu}_B]} \sin^2 \nu_B}{\min\limits_{\nu_F \in [\underline{\nu}_F, \bar{\nu}_F]} \sin^2 \nu_F}, \tag{40}$$

with $0 < \xi < 1$, then there exist a $T \geq 0$ such that

$$\begin{aligned} \|\boldsymbol{e}(t)\| &\leq \|\boldsymbol{e}(t_0)\| e^{-(1-\mu)\lambda(t-t_0)}, \quad \forall t_0 \leq t < t_0 + T, \\ \|\boldsymbol{e}(t)\| &\leq \frac{\eta_\delta \, \bar{\delta} + \eta_{\dot{\theta}_d} \bar{\dot{\theta}}_d}{\mu \lambda}, \qquad\qquad\quad \forall t \geq t_0 + T, \end{aligned} \tag{41}$$

with known constants η_δ, $\eta_{\dot{\theta}_d} > 0$, and rate of convergence

$$\lambda := \xi (1-\epsilon)^2 \min(\kappa_1, \kappa_2). \tag{42}$$

Proof: To prove the bounds for the shoulder-elbow errors $\boldsymbol{e}$, consider the Lyapunov candidate $V = \frac{1}{2} \boldsymbol{e}^\top \boldsymbol{e} > 0$ for all $\boldsymbol{e} \neq \boldsymbol{0}$. Its derivative along (33b) and (33c) is

$$\dot{V} = -\boldsymbol{e}^\top \boldsymbol{M_1} \boldsymbol{e} + \boldsymbol{e}^\top \boldsymbol{M_2} \boldsymbol{\delta} + \boldsymbol{e}^\top \boldsymbol{M_3} \dot{\boldsymbol{\theta}}_{\boldsymbol{d}}, \tag{43}$$

with matrices

$$\begin{aligned} \boldsymbol{M_1} &:= \begin{bmatrix} \kappa_1(1+\eta_{1,1}) & \frac{1}{2}\kappa_1 \eta_{2,1} \\ \frac{1}{2}\kappa_1 \eta_{2,1} & \kappa_2(1+\eta_{2,2}) \end{bmatrix}, \\ \boldsymbol{M_2} &:= \begin{bmatrix} \eta_{1,A} & 0 \\ \eta_{2,A} & \eta_{2,B} \end{bmatrix}, \qquad \boldsymbol{M_3} := \begin{bmatrix} \eta_{1,1} & 0 \\ \eta_{2,1} & \eta_{2,2} \end{bmatrix}. \end{aligned} \tag{44}$$

Then, use Assumption 4 to find the following bounds:

$$\begin{aligned} (1-\epsilon)^2 \leq 1 + \eta_{1,1} \leq (1+\epsilon)^2, \\ (1-\epsilon)^2 \leq 1 + \eta_{2,2} \leq (1+\epsilon)^2, \\ \eta_{1,A} \leq \bar{\eta}_{1,A}, \quad \eta_{2,1} \leq \bar{\eta}_{2,1}, \\ \eta_{2,A} \leq \bar{\eta}_{2,A}, \quad \eta_{2,B} \leq \bar{\eta}_{2,B}, \end{aligned} \tag{45}$$

with constants

$$\begin{aligned} \bar{\eta}_{1,A} &:= i_A \frac{r_A}{d_{AC}} \max_{\nu_F \in [\underline{\nu}_A, \bar{\nu}_A]} \frac{1}{\sin \nu_A}, \\ \bar{\eta}_{2,1} &:= \frac{d_{BC}}{d_{FG}} \max_{\nu_B, \nu_F} \frac{\sin \nu_B}{\sin \nu_F} 4\epsilon, \\ \bar{\eta}_{2,A} &:= -i_A \frac{r_A d_{BC}}{d_{AC} \, d_{FG}} \min_{\nu_A, \nu_B, \nu_F} \frac{\sin \nu_B}{\sin \nu_A \sin \nu_F}, \\ \bar{\eta}_{2,B} &:= i_B \frac{r_B}{d_{FG}} \max_{\nu_F \in [\underline{\nu}_F, \bar{\nu}_F]} \frac{1}{\sin \nu_F}. \end{aligned} \tag{46}$$

Next, define a positive definite matrix

$$\underline{\mathbf{M}}_1 := \xi \begin{bmatrix} \kappa_1(1+\eta_{1,1}) & 0 \\ 0 & \kappa_2(1+\eta_{2,2}) \end{bmatrix}, \tag{47}$$

with $\xi > 0$. Then, use Schur complements, that is Proposition 8.2.4 in [26], and Equation (45) to prove that

$$\left. \begin{aligned} &\xi < 1, \\ &\frac{\kappa_2}{\kappa_1} \geq \frac{\bar{\eta}_{2,1}^2}{4(1-\xi)^2(1-\epsilon)^4}, \end{aligned} \right\} \Longrightarrow \boldsymbol{M_1} - \underline{\mathbf{M}}_{\mathbf{1}} \geq 0. \tag{48}$$

Combine Equations (45) and (48) with the Cauchy-Schwartz inequality $|\boldsymbol{x}^\top \boldsymbol{y}| \leq \|\boldsymbol{x}\| \|\boldsymbol{y}\|$, the definition of compatible norms $\|\boldsymbol{M}\boldsymbol{z}\| \leq \|\boldsymbol{M}\| \|\boldsymbol{z}\|$, and the singular value bound $\|\boldsymbol{M}\| \leq \sigma_{\max}(\boldsymbol{M})$, where $\boldsymbol{x}$, $\boldsymbol{y}$, $\boldsymbol{z} \in \mathbb{R}^n$ and $\boldsymbol{M} \in \mathbb{R}^{n \times n}$, to prove that

$$\dot{V} \leq -\lambda \|\boldsymbol{e}\|^2 + \eta_\delta \|\boldsymbol{e}\| \|\boldsymbol{\delta}\| + \eta_{\dot{\theta}_d} \|\boldsymbol{e}\| \|\dot{\boldsymbol{\theta}}_{\boldsymbol{d}}\|, \tag{49}$$

with constants

$$\begin{aligned} \sigma_{\max}(\boldsymbol{M_2}) \leq \eta_\delta &:= \bar{\eta}_{1,A}^2 + \bar{\eta}_{2,A}^2 + \bar{\eta}_{2,B}^2, \\ \sigma_{\max}(\boldsymbol{M_3}) \leq \eta_{\dot{\theta}_d} &:= \bar{\eta}_{1,1}^2 + \bar{\eta}_{2,2}^2 + \bar{\eta}_{2,1}^2. \end{aligned} \tag{50}$$

Leverage the upper bounds for $\|\boldsymbol{\delta}\|$ and $\|\dot{\boldsymbol{\theta}}_{\boldsymbol{d}}\|$ to write

$$\dot{V} \leq -\lambda \|\boldsymbol{e}\|^2 + \eta_\delta \, \bar{\delta} \, \|\boldsymbol{e}\| + \eta_{\dot{\theta}_d} \bar{\dot{\theta}}_d \|\boldsymbol{e}\|. \tag{51}$$

Then, for any $0 < \mu < 1$

$$\dot{V} \leq -(1-\mu)\lambda \|\boldsymbol{e}\|^2, \qquad \forall \, \|\boldsymbol{e}\| \geq \frac{\eta_\delta \, \bar{\delta} + \eta_{\dot{\theta}_d} \bar{\dot{\theta}}_d}{\mu \lambda}. \tag{52}$$

Algebraic manipulation and the comparison lemma, see Lemma 3.4 in [24], yield the exponential and ultimate uniform bounds in Equation (41). Finally, Equation (48) and Assumption 4 yield the bound on $\frac{\kappa_2}{\kappa_1}$ in this theorem. ∎

Equation (41) limits the allowable disturbances that the system can sustain to maintain uniform ultimate boundedness. In this case, a linear combination of the maximum motor tracking errors and maximum desired joint speeds must be below a certain threshold, which depends on the guaranteed rate of convergence. Notice that as μ approaches 0 and ξ approaches 1, the guaranteed rate of convergence approaches

$\min(\kappa_1, \kappa_2)(1-\epsilon)^2$. Thus, tolerance ϵ reduces the guaranteed rate of convergence. In addition, as ϵ approaches 0 so does $\eta_{\dot{\theta}_d}$. As a result, the ultimate bound in Equation (41) can be decreased using a combination of four strategies: $i)$ improving the performance of the shoulder and elbow motors, that is reducing $\bar{\delta}$; $ii)$ diminishing uncertainties in the geometric characterization of the LSMS, that is decreasing ϵ; $iii)$ slowing down the operations of the LSMS, that is reducing $\bar{\dot{\theta}}_d$; and $iv)$ increasing κ_1 and κ_2. Note, however, that this theorem introduces a constraint on the ratio between the shoulder and elbow gains. An upper bound for T, which depends on the initial errors, can be easily derived using Equation (41).

IV. Test results

Figures 5 through 8 present the results from a test suite designed to evaluate the performance of the algorithm on the LSMS-L35, which is the smaller platform shown in Figure 9. First, the suite steps through a series of scenarios where each joint is checked independently. It concludes with a test that engages all joints simultaneously. The trajectories in these figures are designed to test all the *if else* conditions in Equations (24) and (27). The control law ran at 400 Hz, with the following choice of control gains:

$$\kappa_0 = 1.25, \quad \kappa_1 = 3.50, \quad \kappa_2 = 3.50. \tag{53}$$

Figure 5 shows the results for a trajectory that only moves the waist. As proven in Section III-A, the waist movement is decoupled from the shoulder and elbow dynamics. Accordingly, only the waist signals are presented. Figure 5a depicts the desired and actual joint angles. Figure 5b illustrates the joint error, and confirms accurate tracking is achieved. At the extremum points along the trajectory, the tracking error increases and quickly returns to a small neighborhood around zero. This is caused by a combination of static friction and inertial effects that the controller must overcome when the angular speed of the waist is set to zero. Figure 5c presents the motor commands. Notice the additional control effort used to compensate for the tracking errors occurring at the extrema.

Figure 6 shows the results for a trajectory that only engages the shoulder while the elbow is tasked with maintaining a constant angle. As proven in Section III-A, the shoulder and elbow dynamics are coupled. Accordingly, the figure also contains the elbow signals. As shown in Figure 6a, the trajectory goes through all the possible spreader configurations for cable A, which were detailed in Figure 3. The horizontal bars in the lower part of the figure highlight the spreader configurations for cable A and B. In this case, the geometry of cable A goes through two switches from configuration (a) to (b) and back from (b) to (a) at $t = 86.9$ s and $t = 154.9$ s. The tracking errors for the shoulder and elbow, pictured in Figure 6b, indicate good tracking performance. Figure 6c highlights the coupling between the shoulder and the elbow. As expected from Equation (27), when the shoulder moves a small command is sent to motor B to maintain the elbow angle at zero degrees, due to the shoulder-elbow coupling.

Figure 7 shows the results for a trajectory that only engages the elbow while the shoulder is tasked with maintaining a fixed angle. As highlighted in Figure 7a, the trajectory goes through all the possible spreader configurations for cable B, which were detailed in Figure 4. In this scenario, the geometry of the elbow goes through six configuration switches, as shown by the horizontal bar in the lower part of the image. The errors in Figure 7b show accurate tracking is achieved. The small spikes in the elbow error that appear at the switch points from configuration (b) to (c), and viceversa, are introduced by the Kalman filter that estimates the state of the LSMS. This filter is beyond the scope of this paper, but the discrete nature of the spreader configuration is an added challenge for filtering techniques. These spikes may be reduced with further tuning, or a more sophisticated filter specifically designed for hybrid systems. Figure 7c shows the motor commands. As expected from Equation (24), the movement of the elbow does not affect the shoulder angle. The opposite is true, as seen in Figure 6c.

Last, Figure 8 presents the test results for all joints moving simultaneously. The desired trajectory, shown in Figure 8a, was designed to test the six possible spreader configurations detailed in Equation (27). The horizontal bars on the lower part of the figure cycle through all shoulder and elbow configurations. The errors in Figure 8b exhibit similar patterns to those shown in the individual joint tests. Due to the gear ratio on the different gear boxes, the order of magnitude of the commands for the shoulder and the elbow is much higher than that of the waist, as seen in Figure 8c. To properly visualize the waist command, a second vertical axis has been added on the right side of the figure.

Figures 5 through 8 indicate that the robot successfully tracks complex trajectories that respect the LSMS constraints. Table III provides a summary of the performance parameters used to evaluate the algorithm. The first column provides a list of the tests performed. The second, third, and last columns contain the maximum absolute error, the average absolute error, and the standard deviation from the mean absolute error for the waist, shoulder, and elbow across each of the tests. The maximum tracking errors are below 1.02 degrees for all runs, and the average tracking errors are always below 0.34 degrees. When a specific trajectory requests that a joint angle be kept constant, the desired angle rates are zero. In those scenarios, the trajectory tracking algorithm is leveraged as a position hold controller. As a result, the position hold errors for the waist can be extracted from the shoulder only and elbow only tests. Similarly, the position hold errors for the shoulder and elbow can be retrieved from the waist only test. The position hold errors are always below 0.01, 0.11, and 0.13 degrees for the waist, shoulder, and elbow. As expected, these errors are noticeably smaller than those experienced while attempting to track a dynamic trajectory. These experimental results match the theoretical behavior described in Theorems 1 and 2. Future work may include nonlinear integral terms, or adaptive augmentations to reduce the dynamic errors.

The spreader configuration switches, shown by the horizontal bars on the lower portion of Figures 6 through 8, occur

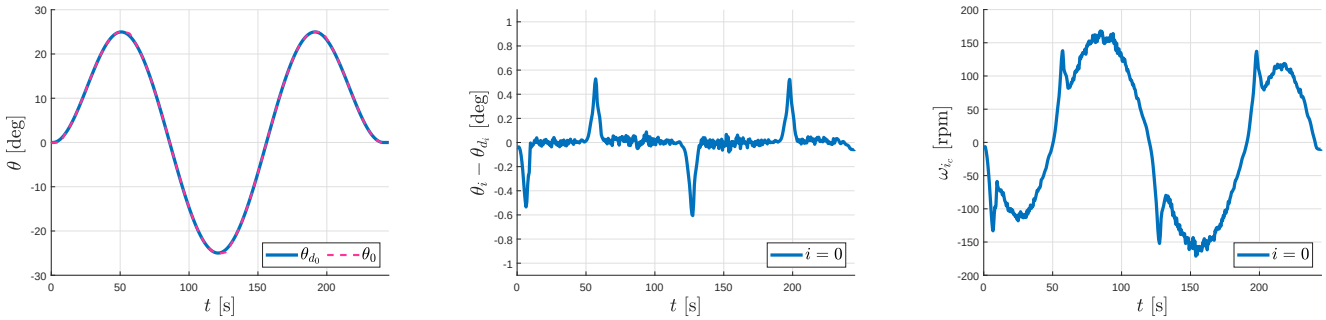

(a) Desired and measured joint angles. (b) Joint angle errors. (c) Motor speed commands.

Fig. 5: Test results on the LSMS-L35 for a trajectory that only engages the waist.

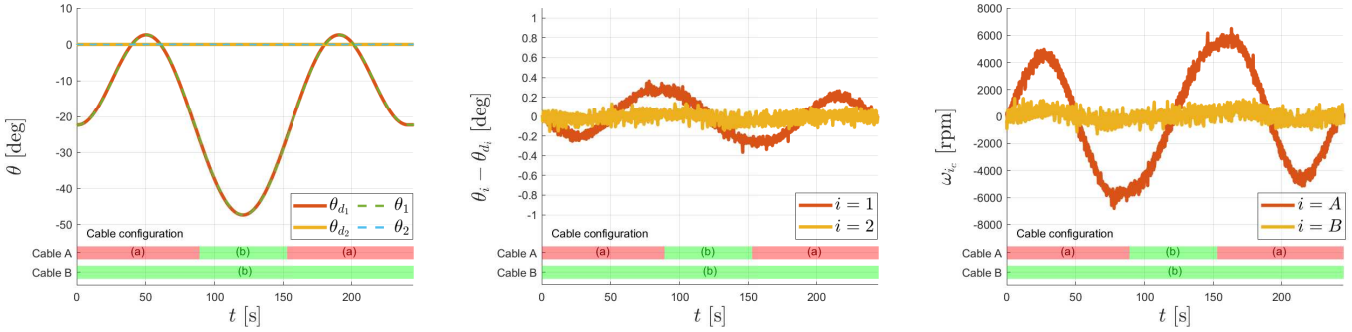

(a) Desired and measured joint angles. (b) Joint angle errors. (c) Motor speed commands.

Fig. 6: Test results on the LSMS-L35 for a trajectory that only engages the shoulder.

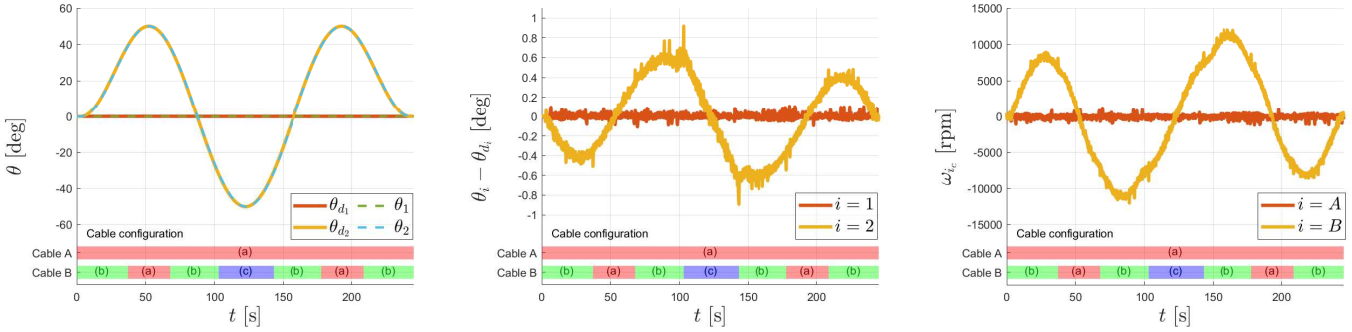

(a) Desired and measured joint angles. (b) Joint angle errors. (c) Motor speed commands.

Fig. 7: Test results on the LSMS-L35 for a trajectory that only engages the elbow.

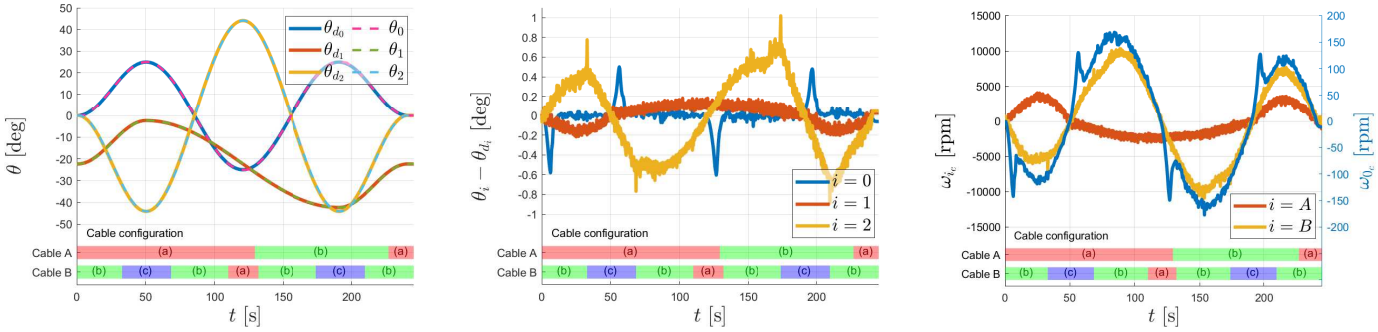

(a) Desired and measured joint angles. (b) Joint angle errors. (c) Motor speed commands.

Fig. 8: Test results on the LSMS-L35 for a trajectory that engages the waist, shoulder, and elbow simultaneously.

TABLE III: Summary of test results.

Test	$\max(\lvert\theta_i - \theta_{d_i}\rvert)$ [deg]			$\mu(\lvert\theta_i - \theta_{d_i}\rvert)$ [deg]			$\sigma(\lvert\theta_i - \theta_{d_i}\rvert)$ [deg]		
	$i=0$	$i=1$	$i=2$	$i=0$	$i=1$	$i=2$	$i=0$	$i=1$	$i=2$
Waist only	**0.606**	0.108	0.127	**0.058**	0.020	0.025	**0.126**	0.026	0.031
Shoulder only	0.007	**0.366**	0.154	0.003	**0.154**	0.034	0.002	**0.175**	0.042
Elbow only	0.006	0.108	**0.919**	0.005	0.018	**0.332**	0.001	0.025	**0.382**
All joints	0.605	0.217	**1.020**	0.052	0.081	**0.327**	0.115	0.093	**0.381**

Fig. 9: LSMS-1000 and LSMS-L35 in the laboratory.

at the angles specified in Table IV. These angles mark where the algorithm believes a configuration switch occurs. Due to modeling errors, these values differ slightly from the actual transition angles, as discussed in Section III-A.

V. Conclusion

This paper proposes a nonlinear, switched control law for a family of cable-driven, articulated robots with long reach. The nonlinearities are caused by the geometry that relates cable lengths to joint angles. The hybrid nature of the problem is introduced by the spreaders and their contact with the cables under certain configurations. Under ideal conditions, this work proves local exponential stability of the angle errors for any feasible trajectory. A global result is not possible due to the physical limits of this family of cranes, which lose controllability of the shoulder and elbow angles when the cables are not under tension. Under realistic assumptions, this work proves that the trajectory tracking errors are uniformly ultimately bounded. A single Lyapunov function was found for this type of hybrid systems, which greatly facilitated the perturbation analysis. While the nonlinear algorithm with switching conditions leads to a more challenging implementation, the linear closed-loop dynamics that result in the ideal case can expedite future developments. For instance, the implementation of an $\mathcal{L}_1$-adaptive augmentation loop that can partially compensate for unmodelled dynamics and external disturbances. Future work should also look into the forces and torques exerted on the structure and how to estimate them, with a special emphasis on unstructured payloads, like lunar regolith. Future efforts should also consider the design of algorithms that directly control the position of the end effector, to ensure payloads can be picked up and delivered autonomously. To this end, the inverse kinemtics of the LSMS [9], which have two possible solutions, are a useful tool to build upon.

TABLE IV: Transition angles for the cable geometry.

Cable	Transition angles	Value [deg]	Spreader contact
A	θ_1^*	-26.07	D
B	θ_2^*	38.93	I
	θ_2^{**}	-31.26	H

Acknowledgments

The authors would like to thank Amelia Scott for the development of the Unscented Kalman filter that makes this work possible; Kevin Anderson and Robert Lorkiewicz for scripting, recording, and editing the video that accompanies this paper; and William Doggett for his advice on the intersection of structures, robotics, and in-space assembly.

References

[1] William Doggett, John Dorsey, Tim Collins, Bruce King, and Martin Mikulas. A versatile lifting device for lunar surface payload handling, inspection & regolith transport operations. *American Institue of Physics Conference Proceedings*, 969(1):792–808, January 2008. doi: 10.1063/1.2845045.

[2] Melanie L. Grande, Robert W. Moses, Patrick A. Cosgrove, Robert P. Mueller, Tracie J. Prater, and Alexander J. Blanchard. Protecting crew and surface systems with a long-duration lunar safe haven. In *ASCEND*, Las Vegas, NV, USA, November 2021. doi: 10.2514/6.2021-4070.

[3] John Dorsey, Martin Mikulas, and William Doggett. Preliminary structural design considerations and mass efficiencies for lunar surface manipulator concepts. In *AIAA SPACE Conference & Exposition*, San Diego, CA, USA, September 2008. doi: 10.2514/6.2008-7916.

[4] Iok M. Wong and Julia E. Cline. LSMS–L35, miniature crane for payload off-loading and manipulation: Development, and application. In *ASCEND*, Las Vegas, NV, USA, October 2022. doi: 10.2514/6.2022-4237.

[5] *Astrobotic Lunar Lander, payload user's guide*. Astrobotics, Pittsburg, PA, USA, 2024. URL https://www.astrobotic.com/lunar-delivery/landers/peregrine-lander/.

[6] Thomas C. Jones. A protoflight lightweight surface manipulation system to enable high-load, long reach lunar surface operations. In *ASCEND*, Las Vegas, NV, USA, November 2021. doi: 10.2514/6.2021-4167.

[7] Blue Origin. Blue Moon, lunar landers. URL https://www.blueorigin.com/blue-moon.

[8] Jacob Martin, Dominic R. Bisio, William D. Chapin, and Erik E. Komendera. Development of a commercialized lightweight surface manipulation system for autonomous operations. In *ASCEND*, Las Vegas, NV, USA, October 2022. doi: 10.2514/6.2022-4370.

[9] William Doggett, Carlos Roithmayr, John Dorsey, Thomas Jones, Bruce King, Martin Mikulas, Haijun Shen, and Hans Seywald. Automation of a versatile crane (the LSMS) for lunar outpost construction, maintenance and inspection. In *AIAA SPACE Conference & Exposition*, Pasadena, CA, USA, September 2009. doi: 10.2514/6.2009-6546.

[10] Lingchong Gao, Chunyu Yu, Jinshuai Xu, Michael Kleeberger, and Johannes Fottner. A survey of lunar cranes and some inspiration from the perspective of Earth crane technology. In *IEEE Annual International Conference on CYBER Technology in Automation, Control, and Intelligent Systems*, Suzhou, China, July 2019. doi: 10.1109/CYBER46603.2019.9066753.

[11] *Technical Description Rail Mounted Gantry Cranes*. Liebherr, Germany, 2020. URL https://www.liebherr.com/en/usa/products/construction-machines/tower-cranes/fast-erecting-cranes/k-cranes/details/71200.html.

[12] Minhnhat Vu, Amadeus Lobe, Florian Beck, Thomas Weingartshofer, Christian Hartl-Nesic, and Andreas Kugi. Fast trajectory planning and control of a lab-scale 3D gantry crane for a moving target in an environment with obstacles. *Control Engineering Practice*, 126 (105255), June 2022. doi: 10.1016/j.conengprac.2022.105255.

[13] Shenghao Tong, Huaitao Shi, Peng Zhou, Wenpo Xu, and Jian Ma. Research on accurate motion control of cable crane based on variable structure sliding mode. *Journal of the Brazilian Society of Mechanical Sciences and Engineering*, 45(316), May 2023. doi: 10.1007/s40430-023-04236-4.

[14] William Doggett, Bruce King, Thomas Jones, John Dorsey, and Martin Mikulas. Design and field test of a mass efficient crane for lunar payload handling and inspection: The lunar surface manipulation system. In *IAA SPACE Conference & Exposition*, San Diego, CA, USA, September 2008. doi: 10.2514/6.2008-7635.

[15] *34K Technical Data*. Liebherr, Germany, 2022. URL https://www.liebherr.com/en/usa/products/construction-machines/tower-cranes/fast-erecting-cranes/k-cranes/details/71200.html.

[16] *The K series, time-tested with a fresh approach*. Liebherr, Germany. URL https://www.liebherr.com/en/usa/products/construction-machines/tower-cranes/fast-erecting-cranes/k-cranes/details/71200.html.

[17] *Manitowoc 18000, Product Guide*. Manitowoc, Wisconsin, USA, 2013. URL https://www.manitowoc.com/manitowoc/lattice-boom-crawler-cranes/18000.

[18] *Hydraulic Crawler Crane CK3300G-2*. Kobelco, Texas, USA. URL https://kcmu-cranes.com/products/ck3300g-2/.

[19] Geir Ole Tysse, Andrej Cibicik, Lars Tingelstad, and Olav Egeland. Lyapunov-based damping controller with nonlinear MPC control of payload position for a knuckle boom crane. *Automatica*, 140(110219), June 2022. doi: 10.1016/j.automatica.2022.110219.

[20] Lingchong Gao, Xiaobing Dai, Michael Kleeberger, and Johannes Fottner. Quasi-static optimal control strategy of lattice boom crane based on large-scale flexible nonlinear dynamics. In *Simulation and Modeling Methodologies, Technologies and Applications*, February 2023. doi: 10.1007/978-3-031-23149-0_9.

[21] Julia Cline, Matthew Vaughan, Walter Waltz, and Iok Wong. LANDO: Developing autonomous surface operations for planetary surfaces. In *AIAA Scitech Forum*, San Diego, CA, USA, January 2022. doi: 10.2514/6.2022-0625.

[22] Kevin D. Earle, Matthew Carrier, William Cirillo, Melanie L. Grande, Christopher A. Jones, Emily Judd, Jordan J. Klovstad, Andrew C. Owens, David Reeves, and Matthew Stafford. *Strategic Framework for NASA's Space Technology Mission Directorate*. September 2018. doi: 10.2514/6.2018-5136.

[23] NASA strategic plan 2022. Technical report, National Aeronautics and Space Administration, March 2022. URL https://www.nasa.gov/wp-content/uploads/2018/01/2022_nasa_strategic_plan_0.pdf.

[24] Hassan K. Khalil. *Nonlinear Systems*. Prentice Hall, Upper Saddle River, NJ, USA, 3rd edition, 2002.

[25] Daniel Liberzon. *Switching in Systems and Control*. Birkhäuser, Boston, MA, USA, 2003.

[26] Dennis S. Bernstein. *Matrix Mathematics*. Princeton University Press, Priceton, NJ, USA, 2nd edition, 2009.